AIAA JOURNAL
Vol. 49, No. 1, January 2011

Periodic Electrodynamic Field of Dielectric Barrier Discharge

P. G. Huang,* J. S. Shang,† and S. A. Stanfield‡
Wright State University, Dayton, Ohio 45435

DOI: 10.2514/1.J050463

The periodic electrodynamic field of a dielectric barrier discharge is investigated via a physically based model and solved with rigorous boundary conditions associated with Maxwell equations for electromagnetics in the time domain. The global motion of charged particles in the form of a succession of random microdischarges is described by the drift-diffusion theory. The plasma-generation process of the dielectric barrier discharge is still mainly the result of avalanche growth of electrons produced by the secondary emission on the cathode. This phenomenon together with the charged-particle accumulation on the electrode will be demonstrated in a two-dimensional simulation as the principal mechanism for generating the so-called electric wind. Through the present approach, the self-limiting characteristic of a dielectric barrier discharge for preventing corona-to-spark transition is convincingly demonstrated.

Introduction

FOR high-speed flow control, some of the magneto-fluid-dynamic interaction is generated by a surface direct current discharge (DCD) through electrostatic force and Joule heating [1]. However, there is a serious limitation imposed by the diffusive DCD to function only in a low-ambient-pressure condition of a few torr [2]. This restriction can be eliminated by using a corona or dielectric barrier discharge [3–8]. Viable flow controls at atmospheric conditions have been demonstrated by using a dielectric barrier discharge (DBD) and corona discharge in subsonic and transonic flow regimes [4,5,7,8]. A promising application for retarding dynamic stall of an airfoil is demonstrated by Post and Corke [7]. They adopt the DBD for surface plasma generation and the relatively small electromagnetic force becomes very effective at the bifurcation point of flow field. This particular gas ionizing process via electronic collision is also known as the silent discharge and has been applied to ozone production since the mid-19th century [9,10].

The DBD operates on a self-limiting process in moderating the electric field strength via the dielectric surface-charge accumulation, therefore prevents the corona-to-spark transition. The partially ionized gas in the electrode gap is generated through a succession of random streamer formations in space and time. In application, the DBD generally operates at atmospheric pressure, for gap lengths on the order of from 1 mm to a few centimeters. At the relatively large value of pressure times gap distance ($p \times d$), the discharge operates in a streamer mode. An alternating voltage is required to support the random transient streamer formation in the electrode gap and quenching by the localized charge buildup on the dielectric layers. In essence, DBD discharges are operated in the microdischarge mode and the streamer discharges whose lifetime is governed by the ionization-recombination process. Therefore, the life cycle of a microdischarge is measured in tens of nanoseconds. Random physical phenomena of such fine scales in time and space are beyond the reach of current computational capability for direct simulation and must therefore be modeled.

The most important feature of flow control using a DBD is that it removes the low-pressure restriction imposed by glow discharges. The nonequilibrium chemical kinetics associated with the DBD is well known and can be thoroughly studied by treating 143 reactions among 30 reacting species [10]. The ionization-recombination process has recently been studied via a chemical kinetic model by Solov'ev et al. [11]. The complex chemical composition of the weakly ionized gas is fully recognized, but the most profound feature for aerodynamic applications is the transport property of electrical conductivity and the electrodynamic force generated by the space charge separation over the electrodes [2]. In spite of a long history of DBD applications, the critically important electromagnetic field structure for magneto-fluid-dynamic interactions is largely unresolved.

Nevertheless, the electro-fluid-dynamic interaction through the inelastic collision process between ion and neutral particles produces a wall-jet-like airstream; the maximum magnitude of the wall jet speed can be as high as a few meters per second [6–8]. This energetic wall jet has been shown to be very effective for flow control [5–8]. Most important, there is also a very limited amount of basic knowledge on the interaction of the charged particles in an electromagnetic field, raising a series of questions on whether the charge separation over the electrode plays a dominant role for the observed plasma motion. The present effort addresses this uncertainty for the electromagnetic field of a DBD by applying the rigorous discontinuous boundary condition for the normal components of the electrical displacement D across the media interface and by balancing the jump with the surface-charge density ρ_s [12].

Governing Equations

In DBD operation, the secondary emission from cathode and Townsend's mechanism controls the multiple primary avalanches ultimately maintains the discharge. Earlier efforts by Massines et al. [13] and Lee et al. [14] gained helpful insights. Most of the early approaches assumed that electrons and ions are in equilibrium with the electric field. In particular, Lee et al. solve the Boltzmann equation for the electron energy distribution function. Both efforts investigated the basic phenomenon during a single ac cycle after the initial transient has subsided. Their two-dimensional analyses were conducted for a parallel-electrode discharge, which is unsuitable for flow control applications. However, all previous investigators understood the key elements of the discharge; the temporal-spatial variation of the physics must be analyzed.

The basic knowledge of DBD has been enriched by the works of Beouf and Pitchford [15], Golubovskii et al. [16], Font [17], and Roy

Presented as Paper 2010-0961 at the 48th AIAA Aerospace Sciences Meeting, Orlando, FL, 4–7 January 2010; received 28 January 2010; revision received 9 September 2010; accepted for publication 9 September 2010.

*Professor and Chair, Department of Mechanical and Materials Engineering Department. Associate Fellow AIAA.
†Research Professor, Department of Mechanical and Materials Engineering Department. Fellow AIAA.
‡Ph.D. Candidate, Department of Mechanical and Materials Engineering Department.

et al. [18] among many others. All their efforts except those of Roy et al. [18] do not describe the chemical kinetics of the excited species and their influence on the plasma generation. Font studies the atmospheric plasma discharge using particle-in-cell and Monte Carlo methods. In their approach, the particle motion is driven by the electric field governed by the Poisson's equation of plasma dynamics with the free-space charges [17]. From these investigations, it becomes very clear that a time-dependent multidimensional description with at least two spatial dimensions is required to resolve a self consistent space charge field. In addition, the depletion of electrons from the dielectric barrier and surface recombination exert a strong influence on the discharge behavior.

The temporal and spatial development of a nonequilibrium partially ionized gas that consists of electrons, ions, and neutral particles can be described by the classic drift-diffusion theory [19,20]

$$\frac{\partial n_e}{\partial t} + \nabla \cdot \Gamma_e = \alpha(|\mathbf{E}|, p)|\Gamma_e| - \beta n_e n_+ \tag{1}$$

$$\frac{\partial n_+}{\partial t} + \nabla \cdot \Gamma_+ = \alpha(|\mathbf{E}|, p)|\Gamma_e| - \beta n_e n_+ \tag{2}$$

Here, $\Gamma_e = -D_e \nabla n_e - n_e \mu_e \mathbf{E}$ and $\Gamma_+ = -D_+ \nabla n_+ + n_+ \mu_+ \mathbf{E}$ are the electron and ion flux densities, respectively. In the above formulation, $\alpha(|E|, p)$ and β are the first Townsend ionization coefficient and recombination coefficient, respectively. The μ_e and μ_+ are the electron and ion mobility, and D_e and D_+ are the electron and ion diffusion coefficients [19]. The current density of the discharge, $\mathbf{J}$, is simply the difference of the ion and electron flux densities, $\mathbf{J} = e(\Gamma_+ - \Gamma_e)$. For the present purpose, the composition of the partially ionized gas is adequately described by the Townsend's formulation for the chemical kinetics. If a more detailed chemical composition of the charge is required, Townsend's correlation can be easily replaced by the chemical kinetic models like that of Elisson and Kogelschatz [10] and Solov'ev et al. [11].

In the globally neutral plasma field, the electrical field intensity can be derived from the electrical field potential, $\mathbf{E} = -\nabla\varphi$. Gauss's law for the electrical displacement leads to the Poisson equation for the electrical field to ensure a self consistent electrical field for a DBD:

$$\nabla^2 \varphi = \frac{e}{\varepsilon}(n_e - n_+) \tag{3}$$

where e is the elementary charge and ε is the electrical permittivity, which is different for a weakly ionized gas and a dielectric. The typical relative dielectric permittivity for dielectric materials has a range from 2.7 (polystyrene) to 6.0 (lead glass).

The media interface boundary conditions for a DBD consist of two principal groups; the exposed electrode and the encapsulated electrode or the dielectric surface. The physical meaningful boundary condition for the former is straightforward, because the DBD still is mainly the Townsend discharge. The only difference from the DCD is that in the ac field the electrodes alternatively function as the cathode and anode. The necessary and sufficient boundary conditions on the electrodes for a DCD have been well-established and thus are not the focus of the present analysis [19,20]. On the other hand, the alternating boundary conditions for the exposed and encapsulated electrode offer serious challenge. In short of a microscopic description for different mechanisms of surface-charge absorption, accumulation, recombination, and emission from the dielectric barrier; the boundary conditions on the dielectric shall be imposed according to the theory of electromagnetics [21].

The exposed electrode alternatively acts as the cathode (when the applied electrical potential has a negative polarity) and anode (when the electric potential on exposed electrode is positive). As a consequence, the role of the dielectric surface is directly opposite to that of the exposed electrode, even if the encapsulated electrode is grounded. The following approximate and key boundary conditions have been demonstrated to be robust, and they accurately describe the behavior of the weakly ionized gas as documented in [19,20].

On the cathode surface of the negative polarity phase,

$$\varphi(t) = \mathrm{EMF}\sin(\varpi t) \le 0 \tag{4a}$$

Except for a grounded encapsulated electrode,

$$\varphi(t) = 0 \tag{4b}$$

$$\Gamma_e \cdot \mathbf{n} = -\gamma \Gamma_+ \cdot \mathbf{n} \tag{5}$$

$$\mathbf{n} \cdot \nabla n_+ = 0 \tag{6}$$

The secondary-emission boundary condition described by Eq. (5) is critical for DBD operation, because it imposes the surface-charge separation by physical observation and it is also the fundamental phenomenon of a DBD and DCD [2].

On the anode surface,

$$\varphi(t) = \mathrm{EMF}\sin(\varpi t) \tag{7}$$

$$n_+ = 0 \tag{8}$$

$$\vec{n} \cdot \nabla n_+ = 0 \tag{9}$$

where EMF is the electrical motive force imposed by the alternative circuit with a frequency of ω. The magnitude of the electrical field potential within the discharge field is determined by satisfying the external circuit equation $\mathrm{EMF}\sin(\varpi t) = \varphi + R\int \mathbf{J}\,\mathrm{d}v$ [19]. The parameter γ is the coefficient of secondary electron emission and has a strong dependency on the material of electrode and the intensity of the electric field. This coefficient associated with the electron collision phenomenon has been continuously investigated, even today, but remains an open issue. Nevertheless, for the drift-diffusion model, a range of values from 10^{-1} to 10^{-2} has been commonly used for weakly ionized air [19,20].

According to the theory of electromagnetics, the electric field across the dielectric and plasma interface must satisfy the following conditions:

$$\mathbf{n} \times (E_d - E_p) = 0 \tag{10}$$

$$\mathbf{n} \cdot (D_d - D_p) = \rho_{e,s} \tag{11}$$

In the above equations, subscripts d and p designate the variable either resides on the dielectric or in the plasma medium. Equation (10) simply states that the tangential electrical field strength is continuous across the media interface. It can be shown in Cartesian frame that the rate of change of the electric potential in z, $\partial\varphi/\partial z$, must be identical across the interface along the x coordinate. Similarly, the rate of change of electrical potential in x, $\partial\varphi/\partial x$, must be equal along the z coordinate across the media interface. For the present simulation, this requirement is automatically satisfied by the definition of two-dimensionality.

The dielectric surface is defined as an impermeable interface of media. All charged particles that reach this boundary are collected on the surface. The boundary condition on the encapsulated electrode can be imposed according to Maxwell equations [12,21]. On the dielectric barrier interface surface, the discontinuity of normal components of the electric displacement must be balanced by the surface-charge density ρ_s. For a DBD, the surface-charge accumulation and depletion plays a controlling role in the self-limiting feature for transition from discharge to spark:

$$\mathbf{n} \cdot [(\varepsilon \mathbf{E})_d - (\varepsilon \mathbf{e})_p] = \rho_s \tag{12}$$

The surface charge can be calculated self-consistently by integrating the electron and ion flux densities, Eqs. (1) and (2), toward the surface. On each surface element the recombination is

supposed to be instantaneous [15]. According to Golubovskii et al. [16], the rate of surface discharge shall include the surface diffusion and desorption by the collisions of excited molecules with the dielectric surface:

$$\Gamma_e|_w = -\gamma\Gamma_i|_w + \rho_e e^{(-E_{\text{binding}})/\kappa T_w} \tag{13}$$

On the dielectric interface, the surface diffusion and desorption can be modeled by the collisions of excited molecules and atoms using their collision frequency and the binding energy [16]. However, for the present purpose, the added sophistication is not included. Therefore, the charge accumulation on the surface is solely results from the instantaneous recombination of the positive and negative charged particles, and Eq. (12) reduces to a simpler formula. This equation can be further developed by introducing the electric potential $E = -\nabla\varphi$ to become

$$\varepsilon_p \frac{\partial\varphi_p}{\partial n} - \varepsilon_d \frac{\partial\varphi_d}{\partial n} = \rho_{e,s} \tag{14}$$

Whence the charge accumulation on the surface is simplified by the instantaneous recombination of the positive and negative charged particles, and Eq. (14) reduces to the following for the two-dimensional formulation:

$$\frac{\partial\varphi_p}{\partial y} = \frac{\varepsilon_d}{\varepsilon_p}\frac{\partial\varphi_d}{\partial y} + \frac{e}{\varepsilon_p}\int (n_i - n_e)\,\mathrm{d}x \tag{15}$$

The above boundary condition clearly reveals the self-limiting characteristic of the DBD in an ac circuit. The accumulated surface charge effectively reduces the electrical field intensity to prevent the corona-to-spark transition. The effective electrical field intensity on the cathode is therefore replaced by Eq. (15) to reflect the true electrical field potential that has been modified by the surface-charge accumulation: either the negative or the positive charges. The instantaneous boundary conditions on the exposed electrode and the dielectric surface are correctly described as a cathode by Eqs. (5), (6), and (15), as well as when acting as an anode by Eqs. (7–9), alternatively, according to the phase of the ac circuit.

Numerical Procedure

For the present investigation the temporal accuracy is essential; therefore, a larger time step using an implicit scheme is not necessary. Instead, a successful iterative relaxation procedure is selected [22]. In this formulation, all electrodynamic equations, including the Poisson equation, can be cast in the flux vector form. As a consequence, the difference between temporal advancement and iterative accuracy is diminished. The governing equations; Eq. (1) and (2), as well as the Poisson equation of plasma dynamics, Eq. (3), can be cast into the flux vector form [20]:

$$\frac{\partial U}{\partial t} + \frac{\partial F_x(U)}{\partial x} + \frac{\partial F_y(U)}{\partial y} = \frac{\partial G_x(U)}{\partial x} + \frac{\partial G_y(U)}{\partial y} + S \tag{16}$$

where the dependent variables, the flux vectors, and the source terms of the present two-dimensional formulation are

$$U = \begin{bmatrix} \phi \\ n_e \\ n_+ \end{bmatrix}, \qquad F_x(U) = \begin{bmatrix} 0 \\ -\mu_e n_e E_{e,x} \\ \mu_+ n_+ E_{+,x} \end{bmatrix}$$

$$F_y(U) = \begin{bmatrix} 0 \\ -\mu_e n_e E_{e,y} \\ \mu_+ n_+ E_{+,y} \end{bmatrix}, \qquad G_x(U) = \begin{bmatrix} \frac{\partial\phi}{\partial x} \\ D_e \frac{\partial n_e}{\partial x} \\ D_+ \frac{\partial n_+}{\partial x} \end{bmatrix}$$

$$G_y(U) = \begin{bmatrix} \frac{\partial\phi}{\partial y} \\ D_e \frac{\partial n_e}{\partial y} \\ D_+ \frac{\partial n_+}{\partial y} \end{bmatrix}, \qquad S = \begin{bmatrix} -\frac{e}{\varepsilon}(n_e - n_+) \\ \alpha|\Gamma_e| - \beta n_e n_+ \\ \alpha|\Gamma_e| - \beta n_e n_+ \end{bmatrix}$$

$$|\Gamma_e| = \sqrt{\left(\mu_e n_e \frac{\partial\phi}{\partial x} - D_e \frac{\partial n_e}{\partial x}\right)^2 + \left(\mu_e n_e \frac{\partial\phi}{\partial y} - D_e \frac{\partial n_e}{\partial y}\right)^2}$$

The delta formulation of the discretized equation, as shown in the following, is used to linearize Eq. (16):

$$\begin{aligned} \Delta F_x &= F_x^{n+1} - F_x^n \approx A_x^n \Delta U, \qquad \Delta F_y = F_y^{n+1} - F_y^n \approx A_y^n \Delta U \\ \Delta G_x &= G_x^{n+1} - G_x^n \approx B_1^n \frac{\partial \Delta U}{\partial x} + B_2^n \frac{\partial \Delta U}{\partial y}, \quad \text{and} \\ \Delta G_y &= G_y^{n+1} - G_y^n \approx B_1^n \frac{\partial \Delta U}{\partial y} - B_2^n \frac{\partial \Delta U}{\partial x} \end{aligned} \tag{17}$$

where n is the iteration level. It should be noted that in the current formulation, the equations are purposely decoupled to render the offdiagonal elements to be zero, and thus these equations can be solved in a sequential manner.

By dropping the time-dependent term and by substituting Eq. (17) into Eq. (16), the equation can be written as

$$\frac{\partial}{\partial x}(\Delta F_x) + \frac{\partial}{\partial x}(\Delta F_y) = \frac{\partial}{\partial x}(\Delta G_x) + \frac{\partial}{\partial y}(\Delta G_y) + R^n \tag{18}$$

where

$$R^n = -\frac{\partial}{\partial x}(F_x^n) - \frac{\partial}{\partial x}(F_y^n) + \frac{\partial}{\partial x}(G_x^n) + \frac{\partial}{\partial y}(G_y^n) + S^n$$

It should be noted that the right-hand side of Eq. (18) is explicit and it can be evaluated using the intermediate solution with any high-order scheme, provided it is numerically stable. In the current study, a central-differencing scheme for the diffusive and source terms is employed. Meanwhile, a quadratic upwind-differencing scheme is adopted for the convective terms. The detail treatments will be discussed in the remaining part of this section.

The discretization of the diffusive terms is done by the central-differencing scheme. For example,

$$\frac{\partial}{\partial x}(G_x^n) \approx \frac{G^n_{x_{i+\frac{1}{2},j}} - G^n_{x_{i-\frac{1}{2},j}}}{x_{i+\frac{1}{2}} - x_{i-\frac{1}{2}}} \tag{19}$$

where

$$\begin{aligned} G^n_{x_{i+\frac{1}{2},j}} &= B_1\left(\frac{\partial U}{\partial x}\right)^n_{i+\frac{1}{2},j} + B_2\left(\frac{\partial U}{\partial y}\right)^n_{i+\frac{1}{2},j} = B_1 \frac{U^n_{i+1,j} - U^n_{i,j}}{x_{i+1} - x_i} \\ &+ B_2 \frac{(U^n_{i,j+1} + U^n_{i+1,j+1})/2 - (U^n_{i,j-1} + U^n_{i+1,j-1})/2}{y_{j+1} - y_{j-1}} \end{aligned} \tag{20}$$

In contrast, the convective flux is discretized by a high-order upwind-differencing scheme. For example,

$$\frac{\partial}{\partial x}(F_x^n) \approx \frac{F^n_{x_{i+\frac{1}{2},j}} - F^n_{x_{i-\frac{1}{2},j}}}{x_{i+\frac{1}{2}} - x_{i-\frac{1}{2}}} \tag{21}$$

where

$$F^n_{x_{i+\frac{1}{2},j}} = \tfrac{1}{2}A^n_{x_{i+\frac{1}{2},j}}\left(U^n_{R_{i+\frac{1}{2},j}} + U^n_{L_{i+\frac{1}{2},j}}\right) - \tfrac{1}{2}|A^n_{x_{i+\frac{1}{2},j}}|\left(U^n_{R_{i+\frac{1}{2},j}} - U^n_{L_{i+\frac{1}{2},j}}\right) \tag{22}$$

The values of $U_{R_{i+\frac{1}{2},j}}$ and $U_{L_{i+\frac{1}{2},j}}$ are obtained by a high-order upwind Lagrange interpolation from the values of U at the nodal point values $U'_{i,j}s$ to the interface location $(x_{i+1/2}, y_j)$. The subscripts R and L represent the upwind interpolation from the right- and left-hand sides, respectively. In the present paper, a quadratic upwind-differencing scheme is used; for example, $U_{R_{i+\frac{1}{2},j}}$ is obtained by the interpolation of a quadratic polynomial constructed by $U_{i,j}$, $U_{i+1,j}$, and $U_{i+2,j}$ at the (x_i, y_j), (x_{i+1}, y_j), and (x_{i+2}, y_j) locations, respectively, and $U_{L_{i+\frac{1}{2},j}}$ is evaluated by the interpolation of a quadratic polynomial constructed by $U_{i-1,j}$, $U_{i,j}$, and $U_{i+1,j}$ at (x_{i-1}, y_j), (x_i, y_j), and (x_{i+1}, y_j) locations, respectively. Finally, the

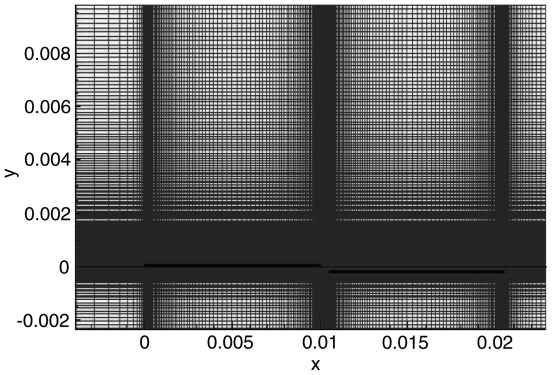

Fig. 1 Typical mesh system for DBD simulation.

ionization rate as appeared in S is evaluated explicitly by the central-differencing scheme approximated at the nodal point, (x_i, y_j).

In the present formulation, all diagonal terms of the discretization are moved to the left-hand side of the finite-difference approximation to maintain diagonal dominance and to enhance the computational stability [20,22]. To improve temporal accuracy, a third-order Runge–Kutta scheme is applied to resolve the rapid variation of the ac discharge in the kHz range. By this formulation, the axiom of the optimal numerical simulation is fully realized in that the physical fidelity is controlled by the accurate right-hand side of the approximation. The left-hand side of the approximation is purely numerical and is constructed to maintain the computational stability [22].

For the present DBD simulations, the ac cycle is limited to a frequency of 10 kHz, and the externally applied electrical field is as high as 4 kV. The overlapping gap distance between the exposed electrode and the dielectric barrier surface has a range up to 3 mm. For this DBD configuration, a typical rectangular mesh system is presented in Fig. 1. The exposed and the encapsulated electrodes have the same dimensions of a length of 10 mm and a thickness of 0.102 mm. The horizontal separation distance between electrodes is 0.5 mm and the encapsulated electrode is embedded in polystyrene by a vertical recess of 0.127 mm. The grid spacing is highly clustered over the electrodes and the adjacent domain between electrodes and gradually stretches toward the far field. The minimum grid spacing in x is 10^{-3} mm, so the electrode is defined by 100 mesh points with clustering at the edges. The minimum grid spacing in the y direction is less than 3.0×10^{-4} mm immediately adjacent to the electrodes.

For two-dimensional computations, the electromagnetic field is assumed to be invariant in the direction of the z coordinate. All interesting information of the electromagnetic field therefore resides within the x-y plane. Since the applied electrical field intensity spans a range from 2 to 4 kV and is maintained by an alternating current at a frequency of 10 kHz, it is a time-dependent phenomenon. For the DBD electrode configuration, a high grid-point density is required in the contiguous region between electrodes and at the edges of electrodes. Three different grid systems were used to generate the preliminary results and the grid dimensions were 192×302, 382×602, and 762×1202. The extremely high temporal and space resolution is required at the instant of discharge breakdown to maintain computational. It is found that the numerical resolution supported by the coarsest grid system of 192×302 has met and exceeded the minimum accuracy requirement to become the mainstay of the present computations.

Numerical Results of DBD

The present numerical results include the discharge characteristic associated with a range of externally applied electrical field potentials. Specifically, the effect of electrode placements to the breakdown voltages is studied. A verification of the voltage-current relationship during the discharge by comparison with experimental data is also included. Finally, the sequence of dynamic events during the discharge cycle, the number density of charged-particle distributions, and the electrical field structure will be selectively depicted and delineated.

Figure 2 presents the comparison of the discharge voltage and electric current with the experimental measurement of Stanfield et al. [23,24] at the externally applied electric field of 2 kV. For this study, the exposed electrode is overlapped over the dielectric surface and separated by a dielectric layer with a thickness of 0.127 mm. Under this condition, the voltage is beneath the breakdown threshold and only the displacement current flows in the electrical circuit. The present computational result predicts correctly the physical behavior as observed by the experiments. Both results indicate a very low displacement electric current, less than 0.008 mA/cm, and the voltage and current are out of phase.

The fundamental self-limiting characteristic of a DBD is convincingly captured by the present results using three different grid densities as shown in Fig. 3. The discharge breakdown takes place before the externally applied electrical potential reaches its peak values for both polarities. Then a lower and constant electric potential results by the conductive current movement within the discharge. According to the numerical simulation, the breakdowns take place before the maximum applied electrical potential. For the positive polarity phase, the discharge occurs when the potential is positive-going and continues until the negative-going external field falls below the threshold of the breakdown value. The identical behavior is also observed for the negative polarity phase. During the initial breakdown process, a sudden drop of the electric field intensity with respect to time induces a surge of the displacement current in the discharge. In experimental measurements, this surge has been known to lead to a train of pulsations of the measured current signature in the electric circuit [4–6] in addition to the multiple microdischarges or streamers. Similarly, the sudden drop of the electrical field potential has also generated nonphysical numerical oscillations in some numerical simulations [25–27].

Figure 4 summarizes the relationship between the breakdown voltage and the gap distance of the exposed and the encapsulated electrodes. Three simulations are produced under the identical externally applied ac electrical field potential of 3.0 kV. The gap distances between electrodes are varying from a contiguously overlapping position to the distance from one to three millimeters.

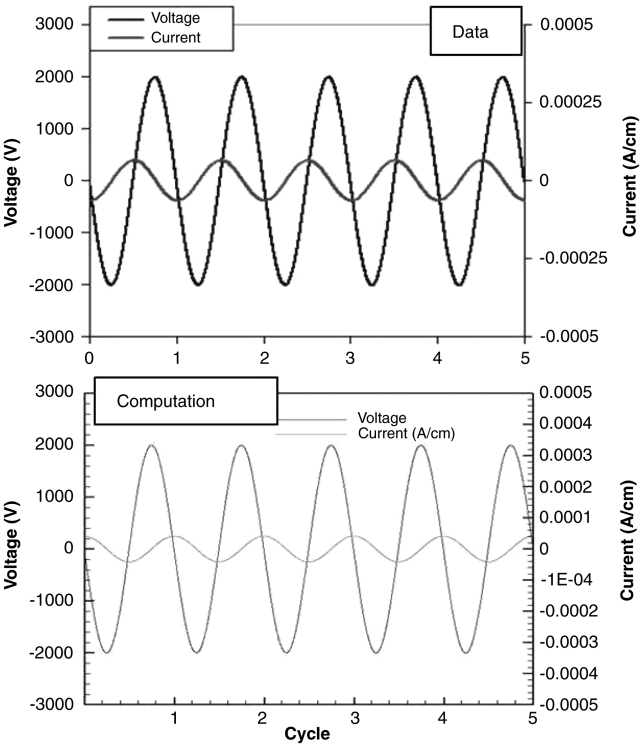

Fig. 2 Comparison of computational and experimental result; $\phi =$ 2.0 kV and $D_{\text{gap}} = 0.0$.

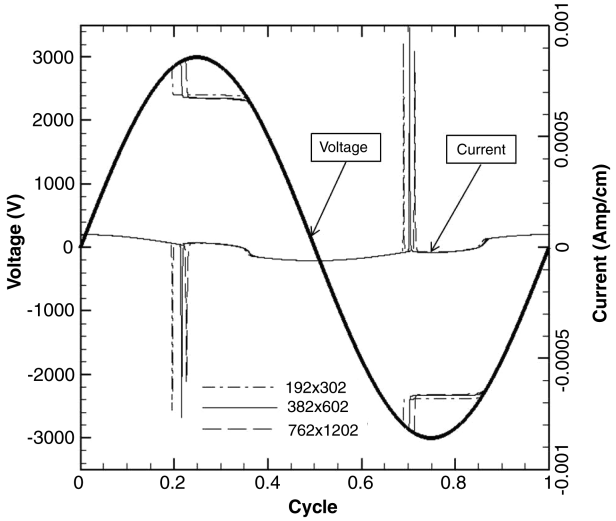

Fig. 3 Numerical resolution of DBD; $\phi = 3.0$ kV and $D_{\text{gap}} = 0.0$.

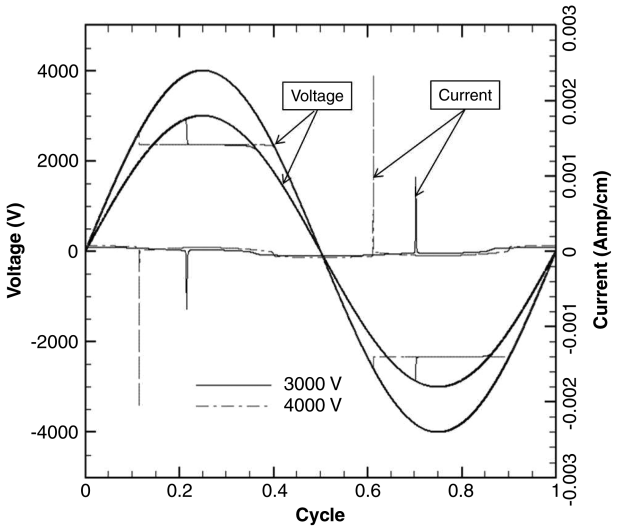

Fig. 5 Breakdown voltage versus externally applied electric field potential.

The surge of the displacement currents at the breakdown is clearly displayed at the discharge breakdown for all three different electrode placements. The breakdown voltages of different gap distances increase as the distance is increased. The lowest breakdown voltage is 2.8 kV when the gap distance vanishes, and the highest voltage is around 2.98 kV when the gap distance is raised to 3.0 mm. Therefore, the breakdown voltage coincides with the peak externally applied voltage. These observations are identical for both the positive and negative polarities of the ac cycle. The important observation from these numerical results is that the computational results honor Paschen's law: for a fixed product of the ambient pressure and the gap distance, $p \times d$, the breakdown voltage is also fixed [2]. For all simulations in the present analysis, the pressure remains at a constant value of 1 atm. Therefore, the important parameter, the quotient E/P for an energy gain between collisions for ionization, is exclusively dependent on the electric field intensity in the present simulations.

Again the constant breakdown voltage at a fixed electrode gap distance predicted by the present drift-diffusion model is depicted in Fig. 5. For these simulations, the placement of the exposed electrode is overlapping over the dielectric barrier surface by a small distance of 1 mm. Under this arrangement, the breakdown voltage indicates a value of 2.8 kV, regardless of the different values of the externally applied electrical field intensity of either 4.0 or 3.0 kV. From these and other computational results in Figs. 3 and 4, the conductive electrical current, although minuscule, is seen only exist during the discharge and vanishes when the applied field voltage is beneath the breakdown value. This numerical behavior has revealed the fact that elevating the applied ac voltage may not increase the magnitude of the electrodynamic force without an upper bound. Within the breakdown limit of the dielectric barrier, the electrodynamic force is linearly proportional to the externally applied voltage and any additional increment is derived from the extended discharge duration at a higher applied voltage.

The comparison of the voltage and electrical current relationship and discharge breakdown with experimental observation is presented in Fig. 6. The computational simulation is generated under the identical conditions as the DBD experiment; the externally applied electric field is 4.0 kV and is operating at a frequency of 10 kHz and the exposed electrode is overlaid on the dielectric barrier surface. The discharge breakdown in the positive polarity is reflected by the single spike in the displacement current of the computational result and by a train of pulses in the experimental observations [4–6,8,23,24]. The computational result correctly captures the induced displacement electrical current by the sudden drop of the electrical potential at the breakdown, according to the Maxwell equation (Faraday's induction law). On the other hand, the experimental data reveals the fundamental multiply microdischarges or streamers of DBD. Experimental

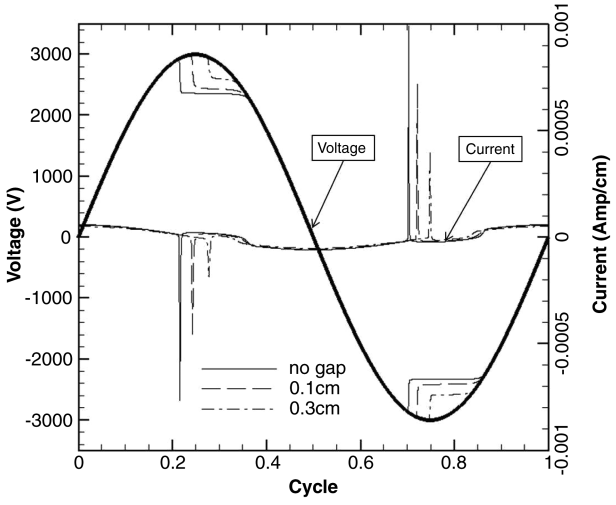

Fig. 4 Dependency of breakdown voltage with respect to gap distance.

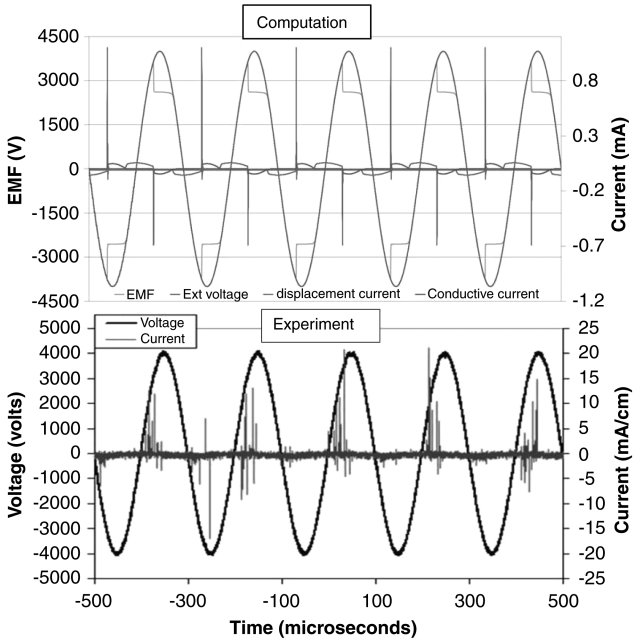

Fig. 6 Comparison of computational and experimental result; $\phi =$ 4.0 kV and gap = 0.0.

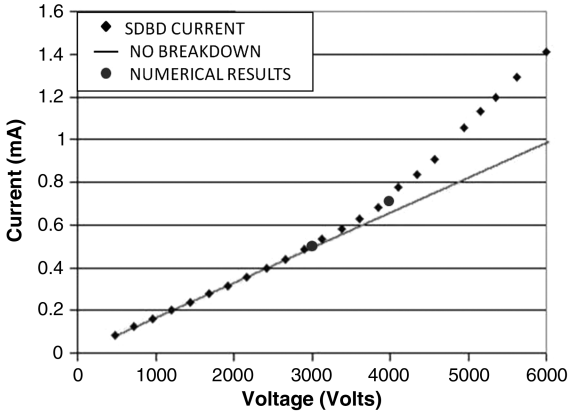

Fig. 7 Comparison of electrical voltage and current data for DBD.

results also indicate a distinctively different pattern between the onsets of discharge breakdown for the positive-going and negative-going voltages. This phenomenon has been pointed out by Enloe et al. [28] and they have shown its results from the altered fundamental characteristic of the microdischarges of the DBD between the two phases. This kind of detail in microdischarge structure is beyond the means of the current state-of-art computational simulations, but the global behavior has been duplicated by the present simulations.

Figure 7 depicts experimental data of the electrical current magnitude versus applied voltage over 512 ac cycles [24]. The solid line denotes the constant displacement electrical current within the ac circuit for voltage magnitudes from 0.5 to 6 kHz. When the measured total electric current departs from the straight line it is an indication that the breakdown occurs. At the breakdown voltage, the magnitude of the conductive current is extremely small, as has also been shown by the computational results. Therefore, it will not be an accurate criterion to determine the breakdown phenomenon. Nevertheless, the calculated conductive electrical current is in general agreement with the experimental data [24]. The integrated conductive electrical current flows through the plasma is less than a few milliamps and is comparable to the magnitude of a direct current discharge [19,20].

The DBD discharge is a periodic and dynamic event. For the present analysis, the characteristic time scale is a short 200 ms for an ac cycle; therefore, meaningful results should be presented at several instants of time. The composite presentation of the number density of ions, electrons, and the net space charge over the dielectric surface, as well as the electric field intensity and electrodynamic force vectors is presented at an instant after the discharge breakdowns in the ac cycle. Figure 8 displays the results shortly after the discharge ignites, when the applied electric field approaches its positive peak. The electrons from the secondary emission are restrained by the propagation of ions to generate a surface accumulation on the dielectric and reduce the intensity of the electric field in the discharge domain. The space charge separation is concentrated in the lower corner region of the exposed electrode above the dielectric surface. The electrodynamic force is exerted in the direction from the exposed to the encapsulated electrode. The predicted overall characteristic of the force field agrees with all experimental observations [6,8]; in that the electrodynamic force produces an acceleration of charged particles for momentum transfer between neutral particles by collision processes. The net result is the appearance of a wall jet. The maximum magnitude of the volumetric force of the present computation is 4.57×10^5 N/m^3 (4.57×10^4 dyne/cm^3) in the cathode layer. The magnitude of this electrostatic force diminishes drastically away from the dielectric barrier surface.

Figure 9 presents detailed temporal sequence of the generation and propagation of electrons via the number density contours, from the time of the breakdown until the discharge ceased. In the positive biased voltage phase of the ac cycle, the discharge lasts for the duration of 41 ms and possesses a physical domain of 0.150 and 0.425 mm in height and length. The discharge domain expands

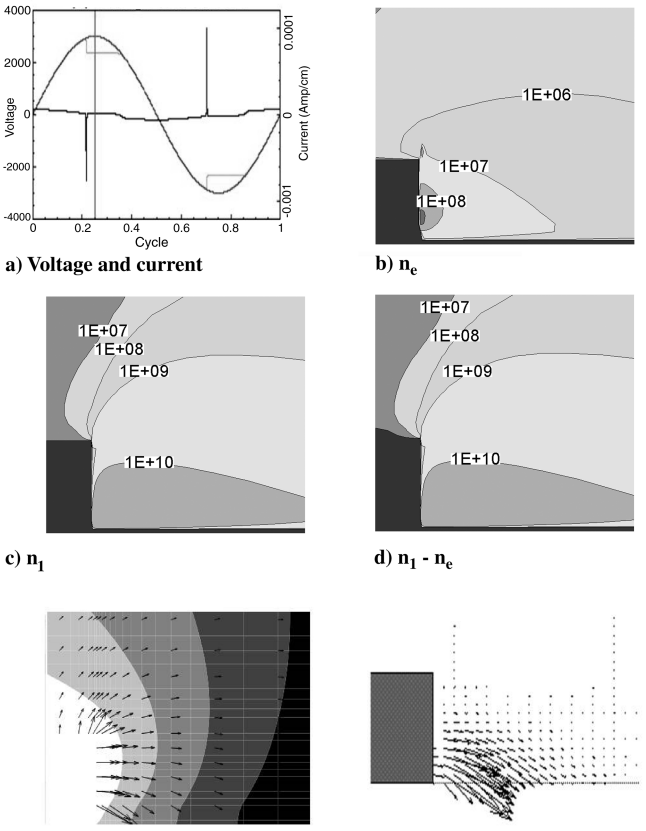

a) Voltage and current

b) n_e

c) n_1

d) n_1 - n_e

e) ϕ and E-field

f) F-vector

Fig. 8 Discharge field after breakdown with positive electrical potential; $\varphi > 0$.

continuously until the externally applied electrical potential falls beneath the breakdown threshold. Constrained by the Derby length, the ion number density distribution is very similar to that of the electron but achieves a maximum value exceeding 10^{10}/cm^3 immediately adjacent to the dielectrics.

Figure 10 depicts the computed results at the instant shortly after breakdown occurs when the externally applied electric potential approaches its negative peak value. Now the electrons propagate away from the exposed electrode (acting as a cathode) over the dielectric surface (behaving as the anode) and the electrical intensity is reduced by the concentration of ions near the lower edge of the exposed electrode; thereby reducing the electric potential in the discharge domain. The electron distribution over the dielectric surface exhibits a more pronounced diffusive pattern than its counterpart when the discharge is associated with positive polarity on the exposed electrode. The distribution of the net space charge separation is also restrained by the slowly moving ions.

This behavior is easily discerned in Fig. 11; from the temporal sequence of the ion number density contours at the instants of breakdown, 3.0, 9.0, 19.0, 29.0, and 40.0 ms afterward. The ions in this phase of ac cycle are expelled from the dielectric surface and propagating toward the exposed electrode. The ion number density has a high concentration to the exposed electrode, and the charge separation domain is confined deeply within the recessed area formed by the overlaid exposed electrode. The discharge domain of ions has almost a constant dimension for the entire breakdown period and vanished as the externally applied electrical potential falls below the breakdown threshold.

The net electrodynamic force reverses its orientation toward the exposed electrode, but the magnitude of the force has a much lower time-averaged magnitude in comparison with the applied electrical potential of positive polarity. The oscillating, but unequal, electrodynamic force generated by the free-space charge separation will be evaluated in the next section.

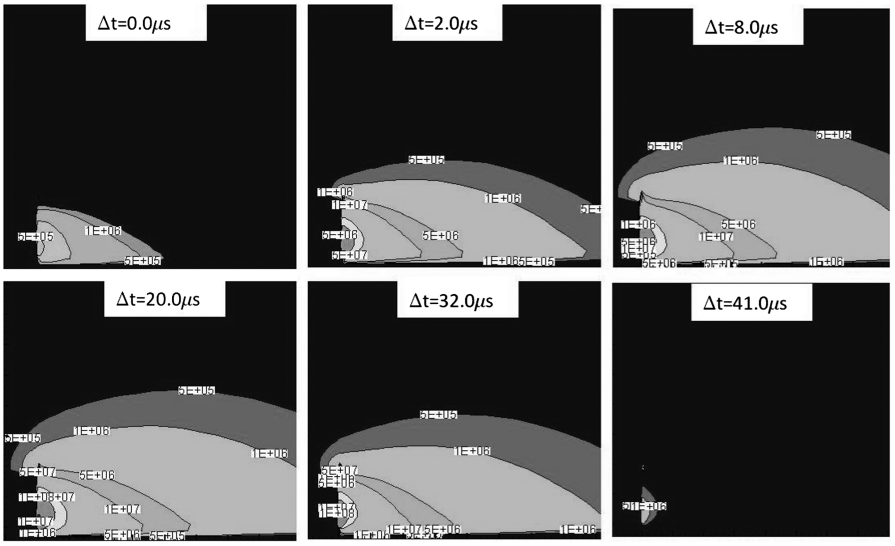

Fig. 9 Temporal sequence of discharge electron number density for $\varphi > 0$.

Electrodynamic Force

For flow control the basic mechanism of a DBD is the electric wind, which is known to associate with the momentum transfer by collisions between the ions and the neutral particles [2–8]. The motion of the charged particles is derived from the electrodynamic force through the interaction of the free-space charge separation and the externally applied electrical field potential. The force acting on the ion in a DBD is of the same nature as in a corona discharge, in fact, the electrode-directed corona discharge is a component of the DBD [2]. The force due to space charge separation is mainly the electrostatic force and can be given as [15,25–27]

$$\mathbf{F} \approx e(n_+ - n_e)\mathbf{E} \tag{23}$$

The force expressed in terms of the electric potential becomes

$$\mathbf{F} = e(n_e - n_+)\nabla\varphi \tag{24}$$

Based on this analytic result, Eq. (24), the orientation of the electrodynamic force is determined by the combined signs of the gradient of the electric potential and the relative magnitude of electron and ion number densities.

The magnitude and orientation of the electrostatic force is controlled by the charge separation in the DBD field. This information can be derived from the instantaneous electron and ion number density distributions and the structure of the electric field potential. Figure 12 displays this information in the DBD field at the instant shortly after the voltage breakdown and the discharge reaches its steady state. Meanwhile, by means of the secondary emission on the cathode, a larger number of ions are accumulated over the dielectric surface; thus, the ion number density is greater than the electron locally. In fact, the computed ion number density distribution has the classic half-Gaussian profile on the dielectric barrier. The maximum value is located near the edge of the exposed electrode next to the dielectric barrier surface and decays away from it. This behavior is known from experiment and has been widely adopted in numerical simulations as input data [26,27]. The instantaneous distribution of $(n_+ - n_e)$ on the dielectric barrier attains a maximum value of 1.08×10^{11} cm^{-3}. According to Eq. (24), the electrostatic force by charge separation originates from the exposed electrode and is directed from the exposed electrode toward the dielectric barrier surface. The instantaneous maximum magnitude of this force is 4.57×10^5 N/m^3 (4.57×10^4 dyne/cm^3) at the juncture between the electrode and dielectric barrier. The computed value is within an order-of-magnitude agreement with the theoretical estimate by Beouf [15]. The average magnitude over an ac cycle is presently undetermined, but the result is expected to be much lower than the instantaneous maximum.

Figure 13 presents the similar instantaneous distributions of the electrical potential and charged-particle number density at the negative peak value of the externally applied electrical field. When the polarity is reversed by the ac field, the sign of the electric potential gradient is now positive from the exposed electrode toward the dielectric barrier. The electric field is also vastly different from the arrangement when the encapsulated electrode is not grounded [7,8]. In this phase of the ac cycle, all ions are repulsed from the dielectric surface, which acts as the anode, and a large number of electrons are

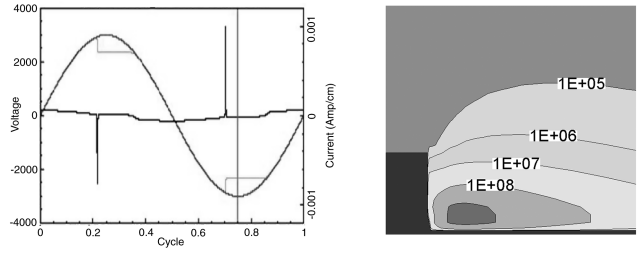

a) Voltage and current

b) n_e

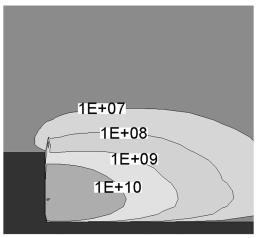

c) n_1

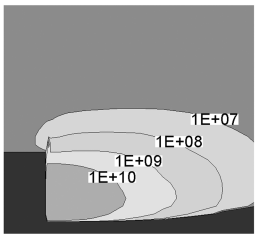

d) n_1 - n_e

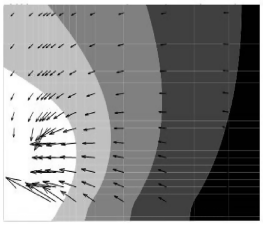

e) ϕ and E-field

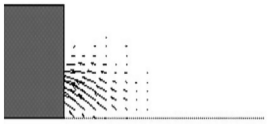

f) F-vector

Fig. 10 Discharge field after breakdown with negative electric potential; $\varphi < 0$.

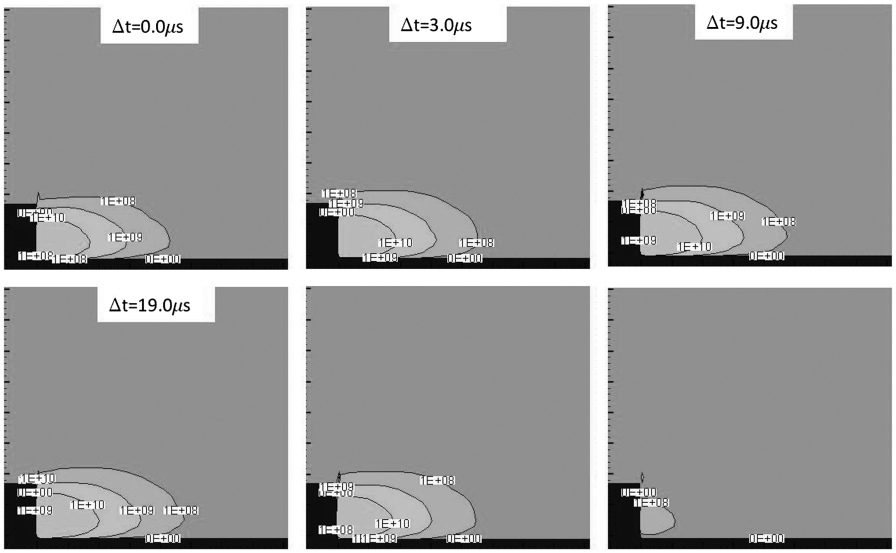

Fig. 11 Temporal sequence of discharge ion number density for $\varphi < 0$.

accumulated over the dielectric barrier surface. According to the present computational results, the plasma sheath is extremely thin (around 0.082 mm) and its thickness decreases with a lower value of the Townsend's electron secondary-emission coefficient. In the innermost juncture region between the electrodes, the number density of ions dominates over that of the electrons and both attain a maximum value of 7.82×10^{10} cm^{-3} and 6.92×10^{10} cm^{-3}, respectively. Inside the sheath but away from the exposed electrode edge, the number density of electrons is overwhelmingly larger than the positively charged ions. Beyond the sheath, the global neutrality of plasma is preserved by the indication that the difference in electron and ion number densities diminishes. According to the present computational result, the negative potential on the exposed electrode is shielded by the plasma sheath from the dielectric barrier and the encapsulated electrode. Above the sheath, the electric field over the exposed and electrically conducting electrode is restored. Deep in the sheath, the sign of $\nabla\varphi$ is positive and the concentration of ions is greater than that of electrons at the junction of the electrodes; thus, the electrostatic force by charge separation is exerted toward the exposed electrode. Away from the exposed electrode edge, the difference of $n_+ - n_e$ becomes negligible over the dielectric surface, although the resultant force again reverses its direction, but its magnitude is also insignificant.

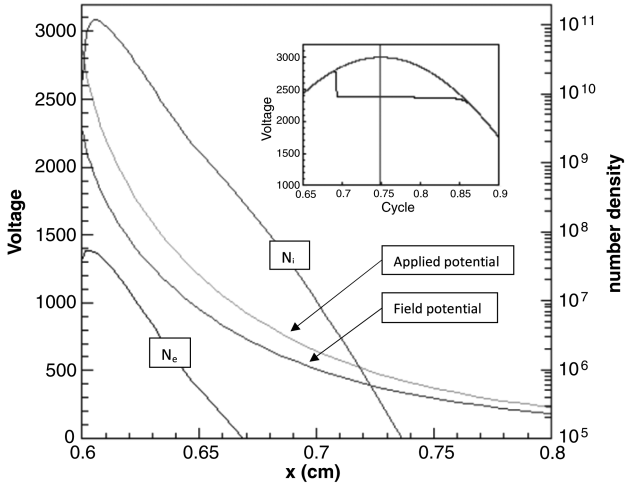

Fig. 12 Instantaneous distributions of electric field potential and charged-particle number density; $\varphi > 0$.

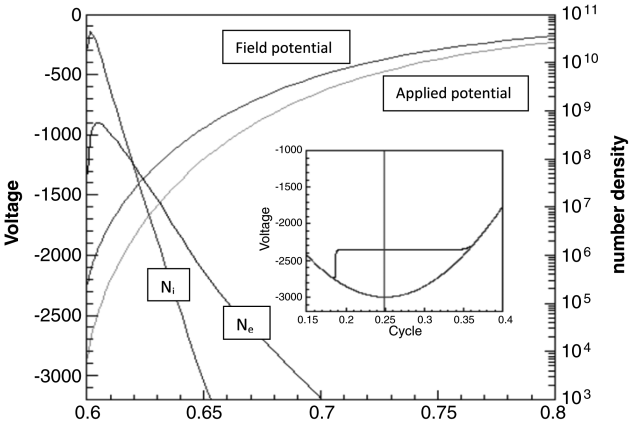

Fig. 13 Instantaneous distributions of electric field potential and charged-particle number density; $\varphi < 0$.

From the present electrostatic formulation and the basic physics of surface discharge accumulation, the direction of the force exerted on the charge particles is from the exposed electrode toward the dielectric barrier in the positive phase of the ac cycle. The orientation of the electrostatic force reverses its direction when the polarity becomes negative. In the jargon of DBD operation, the force is push–pull with a pulse between the switching of polarity [6,28]. Of course, there is a possibility of dynamic transition during the polarity switch, but the magnitude of the force would be negligible, because the decreasing applied electric potential is beneath the breakdown threshold and the discharge ceases [2]. Finally, it must be pointed out that the momentum transfer between the charged and neutral particles can only be taken into account by solving the electrodynamic equations together with the magneto-fluid-dynamic equations.

Conclusions

The dielectric barrier discharge is simulated by solving the electrodynamic equations with a drift-diffusion plasma model using the diagonally dominant, alternating direction implicit scheme via the delta formulation. The stiff governing partial differential equations require exceptional numerical resolution for describing the multiple microdischarges that is beyond the reach of the state-of-the-art computational capability. Therefore, only the global and essential physics of the DBD can be duplicated by using the correct boundary conditions with surface discharge accumulation, which allows the self-limiting corona-spark transition to be convincingly demonstrated.

From the computational results of the surface-charge accumulations and the formulation of electrostatic force, the net force acts on

the charged particle is found to have an alternative orientation from the exposed electrode toward the dielectric barrier surface and the reverse direction according to the negative polarity of the ac cycle. However, the magnitudes of the opposite forces are unequal, and the force is much greater when the exposed electrode has a positive polarity. The maximum instantaneous electrostatic force induced by charge separation is 4.57×10^4 dyne/cm^3. The time-averaged value over a complete alternating current cycle is expected to be much lower and a dominant component of the electrostatic force is directed toward the dielectric barrier surface.

Acknowledgments

The sponsorship of Fariba Fahroo and John Schmisseur of the U.S. Air Force Office of Scientific Research to the present investigation is sincerely appreciated. The authors are thankful for the support from Center of Advanced Power and Energy Conversion, Wright State University (WSU), U.S. Air Force Research Laboratory (AFRL). The authors also are indebted to B. Ganguly of the AFRL and J. Menart of WSU for their fruitful discussions.

References

[1] Shang, J. S., Kimmel, R., Menart, J., and Surzhikov, S. T., "Hypersonic Flow Control Using Surface Plasma Actuator," *Journal of Propulsion and Power*, Vol. 24, No. 5, 2008, pp. 923–934. doi:10.2514/1.24413

[2] Raizer, Y. P., *Gas Discharge Physics*, Springer–Verlag, New York, 1977.

[3] Roth, J. R., Sherman, D. M., and Wilkinson, S. P., "Electrohydrodynamic Flow Control with a Glow-Discharge Surface Plasma," *AIAA Journal*, Vol. 38, No. 7, July 2000, pp. 1166–1172. doi:10.2514/2.1110

[4] Leger, L., Moreau, E., and Touchard, G., "Effect of a DC Corona Electrical Discharge on the Airflow Along a Flat Plate," *IEEE Transactions on Industry Applications*, Vol. 38, 2002, pp. 1478–1485. doi:10.1109/TIA.2002.804769

[5] Artana, G., D'Adamo, J., Léger, L., Moreau, E., and Touchard, G., "Flow Control with Electrohydrodynamic Actuators," *AIAA Journal*, Vol. 40, 2002, pp. 1773–1779. doi:10.2514/2.1882

[6] Enloe, C. L., McLaughlin, T. E., Van dyken, R. D., Kachner, K. D., Jumper, E. J., Corke, T. C., Post, M., and Haddad, O., "Mechanisms and Responses of a Single Dielectric Barrier Plasma Actuator: Geometric Effects," *AIAA Journal*, Vol. 42, 2004, pp. 595–604. doi:10.2514/1.3884

[7] Post, M. L., and Corke, T. C., "Separation Control on High Angle of Attack Airfoil Using Plasma Actuator," *AIAA Journal*, Vol. 42, No. 11, 2004, pp. 2177–2184. doi:10.2514/1.2929

[8] Moreau, E., "Airflow Control by Non-Thermal Plasma Actuators," *Journal of Physics D: Applied Physics*, Vol. 40, 2007, pp. 605–636. doi:10.1088/0022-3727/40/3/S01

[9] Beouf, J. P., "Plasma Display Panels: Physics, Recent Development and Key Issues," *Journal of Physics D: Applied Physics*, Vol. 36, 2003, Paper R53. doi:10.1088/0022-3727/36/6/201

[10] Elisson, B., and Kogelschatz, U., "Nonequilibrium Volume Plasma Chemical Processing," *IEEE Transactions on Plasma Science*, Vol. 19, 1991, pp. 1063–1077. doi:10.1109/27.125031

[11] Solov'ev, V. R., Konchakov, A. M., Krivtsov, V. M., and Aleksandrov, N. L., "Numerical Simulation of a Surface Barrier Discharge in Air," *Plasma Physics Reports*, Vol. 34, No. 7, 2008, pp. 594–608. doi:10.1134/S1063780X08070088

[12] Shang, J. S., "Shared Knowledge in Computational Fluid Dynamics, Electromagnetics, and Magneto-Aerodynamics," *Progress in Aerospace Sciences*, Vol. 38, Nos. 6–7, 2002, pp. 449–467. doi:10.1016/S0376-0421(02)00028-3

[13] Massines, F., Rabehi, A., Decomps, P., Gadri, R. B., Segur, P., and Mayoux, C., "Experimental and Theoretical Study of a Glow Discharge at Atmospheric Pressure Controlled by Dielectric Barrier," *Journal of Applied Physics*, Vol. 83, No. 6, 1998, pp. 2950–2957. doi:10.1063/1.367051

[14] Lee, D., Park, J. M., and Hong, S. H., "Numerical Simulation on Mode Transition of Atmospheric Dielectric Barrier Discharge in Helium-Oxygen Mixture," *IEEE Transactions on Plasma Science*, Vol. 33, No. 2, 2005, pp. 949–957. doi:10.1109/TPS.2005.844493

[15] Beouf, J. P., and Pitchford, L. C., "Electrohydrodynamic Force and Aerodynamic Flow Acceleration in Surface Dielectric Barrier Discharge," *Journal of Applied Physics*, Vol. 97, 2005, Paper 103307. doi:10.1063/1.1901841

[16] Golubovskii, Y. B., Maiorov, V. A., Behnke, J., and Behnke, J. F., "Influence of Interaction Between Charged Particles and Dielectric Surface over a Homogeneous Barrier Discharge in Nitrogen," *Journal of Physics D: Applied Physics*, Vol. 35, 2002, pp. 751–761. doi:10.1088/0022-3727/35/8/306

[17] Font, G. I., "Boundary-Layer Control with Atmospheric Plasma Discharges," *AIAA Journal*, Vol. 44, No. 7, 2006, pp. 1572–1578. doi:10.2514/1.18542

[18] Roy, S., Singh, K. P., and Gaitonde, D. V., "Air Plasma Actuators for Effective Flow Control," AIAA Paper 2007-0184, Reno, NV, 2007.

[19] Surzhikov, S. T., and Shang, J. S., "Two-Component Plasma Model for Two-Dimensional Glow Discharge in Magnetic Field," *Journal of Computational Physics*, Vol. 199, Sept. 2004, pp. 437–464.

[20] Shang, J. S., Huang, P. G., Yan, H., and Surzhikov, S. T., "Computational Electrodynamic Simulation of Direct Current Discharge," *Journal of Applied Physics*, Vol. 105, 2009, Paper 023303. doi:10.1063/1.3066185

[21] Krause, J. D., *Electromagnetics*, McGraw–Hill, New York, 1953, pp. 337–342.

[22] Huang, P. G., "High Order Discontinuity Capturing Using Adaptive Polynomials," AIAA Paper 2006-0305, Reno, NV, 2006.

[23] Stanfield, S. A., Menart, J., DeJoseph, C., Kimmel, R. L., and Hayes, J. R., "Rotational and Vibrational Temperature Distribution for a Dielectric Barrier Discharge in Air," *AIAA Journal*, Vol. 47, 2009, pp. 1107–1115. doi:10.2514/1.37648

[24] Stanfield, S. A., "A Spectroscopic Investigation of a Surface-Discharge-Mode, Dielectric Barrier Discharge," Ph.D. Dissertation, Wright State Univ., Dayton, OH, 2009.

[25] Likhanskii, A. V., Shneider, M. N., Macheret, S. O., and Miles, R. B., "Modeling of Dielectric Barrier Discharge Plasma Actuator in Air," *Journal of Applied Physics*, Vol. 103, 2008, Paper 053305. doi:10.1063/1.2837890

[26] Suzen, Y. B., and Huang, P. G., "Simulations of Flow Separation Control Using Plasma Actuators," AIAA Paper 2006-877, Reno, NV, Jan. 2006.

[27] Shang, J. S., and Huang, P. G., "Simulating Electrodynamic Field of Dielectric Barrier Discharge," AIAA Paper 2008-3777, Seattle WA, June 2008.

[28] EnLoe, C. L., Font, G. I., MacLaughlin, T. E., and Orlov, D. M., "Surface Potential and Longitudinal Electric Field Measurements in the Aerodynamic Plasma Actuator," *AIAA Journal*, Vol. 46, 2008, pp. 2730–2739. doi:10.2514/1.33973

X. Zhong
Associate Editor